Triaxial deformation and nuclear shape transition in ^{192}Au

Y. Oktem,[1] D. L. Balabanski,[2] B. Akkus,[1] L. Amon Susam,[1] L. Atanasova,[2] C. W. Beausang,[3,4] R. B. Cakirli,[1,5] R. F. Casten,[3] M. Danchev,[6,7] M. Djongolov,[6,7] E. Ganioğlu,[1] K. A. Gladnishki,[7] J. Tm. Goon,[8] D. J. Hartley,[6,9] A. A. Hecht,[3,10] R. Krücken,[3,11] J. R. Novak,[3] G. Rainovski,[7] L. L. Riedinger,[6] T. Venkova,[2] I. Yigitoglu,[12] N. V. Zamfir,[3,13] and O. Zeidan[6]

[1]*Department of Physics, Istanbul University, Vezneciler, 34134, Istanbul, Turkey*

[2]*Institute for Nuclear Research and Nuclear Energy, Bulgarian Academy of Sciences, BG-1784 Sofia, Bulgaria*

[3]*Wright Nuclear Structure Laboratory, Yale University, New Haven, Connecticut 06520, USA*

[4]*Department of Physics, University of Richmond, Richmond, Virginia 23173, USA*

[5]*Max-Planck-Institut für Kernphysik, Saupfercheckweg 1, D-69117 Heidelberg, Germany*

[6]*Department of Physics and Astronomy, University of Tennessee, Knoxville, Tennessee 37996, USA*

[7]*Faculty of Physics, St. Kliment Ohridski University of Sofia, BG-1164 Sofia, Bulgaria*

[8]*Louisiana State University Department of Physics and Astronomy 202 Nicholson Hall, Tower Drive, Baton Rouge, Louisiana 70803-4001, USA*

[9]*Department of Physics, U.S. Naval Academy, Annapolis, Maryland 21402, USA*

[10]*Department of Chemistry and Biochemistry, University of Maryland, College Park, Maryland 20742, USA*

[11]*TRIUMF, 4004 Wesbrook Mall, Vancouver, British Columbia V6T 2A3, Canada*

[12]*Gaziosmanpaşa University, Science Faculty, Turkey*

[13]*National Institute for Physics and Nuclear Engineering, Bucharest-Magurele, Romania*

(Received 14 July 2012; published 12 November 2012)

Background: Nuclei in the $A \approx 190$ mass region show gradual shape changes from prolate through nonaxial deformed shapes and ultimately towards spherical shapes as the Pb region is approached. Exploring how this shape evolution occurs will help us understand the evolution of collectivity in this region.

Purpose: The level scheme of the ^{192}Au nucleus in $A \approx 190$ region was studied in order to deduce its deformations.

Methods: High-spin states of ^{192}Au have been populated in the ^{186}W(^{11}B, $5n$) reaction at a beam energy of 68 MeV and their γ decay was studied using the YRAST Ball detector array at the Wright Nuclear Structure Laboratory (WNSL), Yale University.

Results: Based on double and triple γ-ray coincidence data the level scheme of ^{192}Au has been extended up to $I^{\pi} = 32^{+}$ at an excitation energy of $\sim$6 MeV.

Conclusion: The results are discussed in the framework of pairing and deformation self-consistent total Routhian surface (TRS) and cranked shell model (CSM) calculations. The comparison of the experimental observations with the calculations indicates that this nucleus takes a nonaxial shape similar to other Au nuclei in this region.

DOI: 10.1103/PhysRevC.86.054305 PACS number(s): 29.30.Kv, 21.60.Ev, 23.20.Lv, 27.80.+w

I. INTRODUCTION

The gold isotopes have only three proton holes with respect to the $Z = 82$ shell closure, yet the existence of a finite number of valence particles (holes) is able to break the spherical symmetry and introduce deformation. The nuclei with masses $A \approx 190$ lie in a transitional region which is characterized by the presence of different shapes in their ground states, such as prolate, oblate, and triaxial. The lighter isotopes are prolate deformed. By adding more and more neutrons, the shape becomes oblate with the quadrupole deformation parameter β_2 [1] taking values $\beta_2 \leqslant 0.15$ [2–4]. A prolate-oblate shape change has been discussed for these nuclei [5–11]. Recently, the nuclei in this prolate-oblate transition region were described by a potential with similar energy minima corresponding to prolate and oblate shapes [12,13]. The shape transition phenomenon in the case of the platinum ($Z = 78$) nuclei starts at around mass $A = 192$ and persists till $A \approx 200$ [14]. These nuclei are understood to have axially asymmetric shapes and they are considered to present the best examples of γ softness throughout the whole nuclide chart [15].

In the odd-odd ^{190,192,194}Au nuclei two-quasiparticle $\pi h_{11/2}^{-1} \otimes \nu i_{13/2}^{-1}$ rotation-aligned bands with negative parity are known [16,17]. These bands are explained in a framework where the two odd particles, an $i_{13/2}$ neutron and a $h_{11/2}$ proton, are coupled to a γ-deformed core [18]. In the doubly-odd ^{190}Au well developed triaxial shapes were suggested [17] based on a comparison with total Routhian surface (TRS) calculations [19,20].

A partial level scheme of ^{192}Au including a 20^{+} isomeric state was reported previously in Ref. [21]. Here we present a level scheme for ^{192}Au which is extended up to $I^{\pi} = 32^{+}$. We provide a comparison of the experimental data of ^{192}Au with TRS theoretical calculations.

The experimental procedure is described in Sec. II, while the results are listed in Sec. III and are discussed in Sec. IV.

II. EXPERIMENTAL PROCEDURE

High-spin states of ^{192}Au were studied at the ESTU tandem Van de Graaff accelerator at the Wright Nuclear

Structure Laboratory of Yale University. The ^{186}W(^{11}B,5n) heavy-ion fusion evaporation reaction at 68 MeV was utilized to populate high-spin states in ^{192}Au. The target consisted of three 300 μg/cm^2 thickness ^{186}W foils. The cross section of the main 5n evaporation channel (^{192}Au) was calculated to be 570 mb. The emitted γ rays were detected in-beam with the YRAST Ball detector array [22], which consisted of 7 clover detectors, 16 single-crystal Ge detectors, and 3 LEPs detectors for this experiment. The trigger condition required at least three coincident γ rays to deposit their energy in a Clover or in a single-crystal detector. Approximately 10^7 threefold and higher coincidence events were collected, which were sorted into a three-dimensional histogram using the RADWARE package [23].

The analysis of the data involved (i) study of the γ-ray coincidence relationships, (ii) angular distribution and linear polarization measurements in order to deduce the spin and parity of the levels, and (iii) γ-ray intensity measurements.

III. RESULTS

In a previous study of ^{192}Au [21] a partial level scheme was reported. The two-quasiparticle rotational band, which is built on the $\pi h_{11/2}^{-1} \otimes \nu i_{13/2}^{-1}$ configuration, was observed up to $I^\pi = 18^-$. In the present work this sequence was expanded up to $I^\pi = 29^-$ with the level energy of 5708.2 keV. An $I^\pi = 20^+$ isomer [$T_{1/2} = 5.4(3)$ ns, $E_i = 2153$ keV with respect to the 11^- isomer] was established previously [21]. Spin and parity values were assigned to this state in accordance with the systematics of similar structures in the neighboring nuclei, e.g., the 20^+ state in ^{190}Au is an isomer [$T_{1/2} = 6.9(1)$ ns, $E_i = 2172$ keV with respect to the 11^- isomer] [21]. In the present work the sequence built on $I^\pi = 20^+$ isomeric state was established up to $I^\pi = 32^+$ and an energy of 6227.6 keV.

The level scheme of ^{192}Au as established from the present work is presented in Fig. 1. The order of the γ rays is based on coincidence relationships and the measured γ-ray intensities. All transitions that have been observed for ^{192}Au in the present experiment are presented in Table I, together with the energies, the relative intensities, the DCO (directional correlations from oriented states) ratios, $R_{\rm DCO}$, the linear polarization ratios, $A_{\rm pol}$, and the deduced γ-ray multipolarities.

The intensities of all transitions are normalized to the intensity of the 213.4 keV $17^+ \rightarrow 15^+$ transition. The multipolarities of γ ray transitions have been determined from the experimental $R_{\rm DCO}$ and $A_{\rm pol}$ ratios. The $R_{\rm DCO}$ ratio provides information about the spin difference between the levels, while $A_{\rm pol}$ allows one to distinguish between γ rays of electric and magnetic type.

A two-dimensional angular correlation matrix was used to deduce the experimental $R_{\rm DCO}$ ratios,

$$R_{\rm DCO} = \frac{I_{\gamma_i}(\theta_i)\ I_{\gamma_i}(\theta_i : G)}{I_{\gamma_i}(\theta_i)\ I_{\gamma_i}(\theta_i : G)} \frac{\varepsilon_{\gamma_i}(\theta_i)\varepsilon_{\gamma_i}(\theta_i)}{\varepsilon_{\gamma_i}(\theta_i)\varepsilon_{\gamma_i}(\theta_i)}, \qquad (1)$$

where G indicates a gating transition, θ_i, $i = 1, 2$, are the angles at which detectors are placed, ε_{γ_i}, $i = 1, 2$ are the detector efficiencies, and I_{γ_i}, $i = 1, 2$ are the measured γ-ray intensities. To construct this matrix, γ rays detected by a ring of seven clover detectors at 90° with respect to the beam axis were sorted against the other three detectors at 160°. For the DCO analysis, most of the ratios were obtained when gating on the 408.0 keV stretched quadrupole $E2$ transition at the bottom of the level scheme in Fig. 1. If the gate is at a stretched $E2$ transition, the $R_{\rm DCO}$ ratios are greater than 1.0 for $E2$ transitions, approximately 0.7 for stretched $E1$ or $M1$ dipole transitions, and for mixed $M1 + E2$ transitions it takes values in between.

The clover detectors, which are positioned at 90° with respect to the beam in YRAST Ball spectrometer, were used as in-beam Compton polarimeters [24]. At this angle, the polarization is directly proportional to the experimental asymmetry, which is defined as $A_{\rm pol} = (N_\perp - N_\parallel)/(N_\perp + N_\parallel)$ where $N_\parallel$ and $N_\perp$ are the normalized counting rates observed respectively for the coincidences between the Ge crystal acting as scatterer and the horizontal absorber Ge crystal and between the scatterer and the vertical absorber.

In Table I, positive values of the polarization parameter $A_{\rm pol}$ correspond to electric transitions, while negative values reveal pure magnetic transitions. The values for mixed transitions would depend on the dominant component. Information about DCO ratios and polarization coefficients, despite large errors in some cases, was used to fix the spin and parity of most of the levels in ^{192}Au. Sample spectra, revealing the transitions of the different sequences in ^{192}Au are displayed in Fig. 2.

A. Negative parity states in ^{192}Au

The negative parity states are ordered in two sequences, labeled as 1 and 2. The 11^- state is the band head of the negative parity, rotation-aligned $\pi h_{11/2} \otimes \nu i_{13/2}$ band. Sequences 1 and 2 are the favored and unfavored signature branches of this band, which were extended up to $I^\pi = 29^-$ and $I^\pi = 28^-$, respectively.

B. Positive parity states in ^{192}Au

Here we report four positive parity bands labeled as 3, 4, 5, and 6 in Fig. 1, which are built above the 20^+ isomer. Two or three transitions were observed for sequences 3, 5, and 6. The first three transitions of sequence 4 were known [17]. It becomes yrast above $I^\pi = 26^+$ and is extended up to $I^\pi = 32^+$, which is the highest spin state observed in this experiment. Sequence 3 was established in this experiment and was found to decay to sequence 4 via the mixed 497.2-, 546.9- and 689.2-keV $M1/E2$ transitions. It was observed up to $I^\pi = 27^+$. Sequence 5 is built on the known 19^+ state [17] and was established up to $I^\pi = 23^+$. Sequence 6 was observed in this experiment and is built on a 20^+ state which decays to the known 18^+ state [17].

C. Electromagnetic transition probabilities

The establishment of the experimental branching ratios λ,

$$\lambda = T_\gamma(I \rightarrow I - 2)/T_\gamma(I \rightarrow I - 1), \qquad (2)$$

TABLE I. The γ-ray energies, relative intensities, DCO ratios ($R_{\rm DCO}$), polarization ratios ($A_{\rm pol}$), and multipolarity assignments are shown for ^{192}Au as deduced from the ^{186}W(^{11}B,5n) reaction at 68 MeV. The DCO and polarization ratios of some of the transitions could not be measured because of their weak intensities. The intensities are evaluated in a single gate on the 227.8 keV transition. For the DCO analysis most of the ratios were obtained when gating on the 408.0 keV stretched quadrupole $E2$ transition.

E_γ (keV)	E_i (keV)	$I_i^\pi \rightarrow I_f^\pi$	I ($\triangle I$)	$R_{\rm DCO}$ ($\triangle R_{\rm DCO}$)	$A_{\rm pol}$ ($\triangle A_{\rm pol}$)	Multipolarity
68.5[a](1)	2586.3	$20^+ \rightarrow 18^+$				
146.2(1)	3011.1	$20^- \rightarrow 19^-$	9.6(2)	0.88(12)		$M1+E2$
150.9(1)	3162.0	$22^- \rightarrow 20^-$	18.4(1)	1.18(5)		$E2$
154.2(4)	2586.3	$20^+ \rightarrow 18^+$	6.1(1)	1.50(34)		$E2$
166.2(4)	5077.5	$28^- \rightarrow 27^-$	0.5(1)	0.93(31)		$(M1+E2)$
180.2(1)	839.6	$13^- \rightarrow 12^-$	113.8(7)	0.76(4)	−0.03(2)	$M1+E2$
193.2(2)	3787.5	$24^+ \rightarrow 23^+$	7.0(1)	0.67(8)	−0.33(11)	$M1+E2$
203.4(3)	4639.7	$26^+ \rightarrow 25^+$	1.3(1)	0.60(13)		$M1+E2$
204.6(1)	2790.9	$(21^-) \rightarrow 20^+$	8.5(2)	0.71(28)	0.33(30)	$(E1)$
206.3(1)	3289.8	$23^+ \rightarrow 21^+$	12.7(1)	1.06(11)	0.01(15)	$E2$
211.3(3)	2643.4	$19^+ \rightarrow 18^+$	16.3(3)	0.57(4)	−0.31(24)	$M1+E2$
213.4(1)	2176.9	$17^+ \rightarrow 15^+$	100.0(4)	1.14(3)	0.05(4)	$E2$
227.8(1)	659.4	$12^- \rightarrow 11^-$	GATE			$M1+E2$[b]
255.2(2)	2432.1	$18^+ \rightarrow 17^+$	41.8(3)	0.78(2)	−0.14(3)	$M1+E2$
256.1(1)	2864.9	$19^- \rightarrow 18^-$	11.4(1)	0.67(2)	−0.09(3)	$M1+E2$
259.8(1)	1099.4	$14^- \rightarrow 13^-$	157.4(9)	0.76(1)	−0.09(1)	$M1+E2$
272.4(1)	1820.1	$16^- \rightarrow 15^-$	20.2(2)	0.63(4)	−0.19(6)	$M1+E2$
273.1(8)	2790.1	$(21^-) \rightarrow 18^+$	5.0(1)	1.53(25)	−0.17(14)	
291.2(1)	2608.8	$18^- \rightarrow 17^-$	11.1(1)	0.77(6)	−0.14(9)	$M1+E2$
312.6(1)	3985.4	$25^- \rightarrow 24^-$	16.1(2)	0.86(6)	−0.13(9)	$M1+E2$
333.0(2)	4972.7	$28^+ \rightarrow 26^+$	3.6(1)	1.14(8)	0.24(9)	$E2$
334.2(1)	3125.1	$(23^-) \rightarrow (21^-)$	5.3(1)	1.19(46)		$(E2)$
340.9(1)	2517.8	$18^+ \rightarrow 17^+$	67.7(8)	0.89(3)	−0.08(1)	$M1+E2$
356.8(1)	2176.9	$17^+ \rightarrow 16^-$	19.1(2)	0.83(5)	0.10(7)	$E1$
367.7(4)	3011.1	$20^- \rightarrow 19^+$	6.8(1)	0.64(4)	0.13(9)	$E1$
376.5(2)	4853.2	$27^+ \rightarrow 25^+$	3.9(1)	1.13(14)	0.16(12)	$E2$
402.3(1)	3011.1	$20^- \rightarrow 18^-$	24.9(2)	1.06(7)	0.06(5)	$E2$
408.0(1)	839.6	$13^- \rightarrow 11^-$				$E2$[b]
412.6(3)	4398.0	$26^- \rightarrow 25^-$	10.7(1)	0.81(8)	−0.13(9)	$M1+E2$
415.8(2)	1963.5	$15^+ \rightarrow 15^-$	10.7(1)	0.21(5)	−0.22(10)	$E1+M2$
440.0(1)	1099.4	$14^- \rightarrow 12^-$	51.0(3)	1.14(8)	0.05(2)	$E2$
448.3(1)	1547.7	$15^- \rightarrow 14^-$	28.6(2)	0.72(4)	−0.09(3)	$M1+E2$
460.2(10)	4436.3	$25^+ \rightarrow 24^+$	3.2(1)	1.10(16)	−0.04(6)	$M1+E2$
461.1(1)	3047.4	$22^+ \rightarrow 20^+$	45.3(3)	1.20(6)	0.13(2)	$E2$
466.7(1)	2898.8	$20^+ \rightarrow 18^+$	13.3(1)	1.43(27)	0.16(10)	$E2$
473.7(4)	4745.1	$26^+ \rightarrow 24^+$	2.5(1)	1.26(24)	0.20(19)	$E2$
485.6(3)	3610.7	$(25^-) \rightarrow (23^-)$	4.8(1)	1.15(20)	0.36(32)	$(E2)$
497.2(1)	3083.5	$21^+ \rightarrow 20^+$	36.0(4)	0.88(4)	−0.07(3)	$M1+E2$
497.5(10)	2317.6	$17^- \rightarrow 16^-$	16.0(3)	0.69(5)	−0.09(3)	$M1+E2$
497.7(5)	3787.5	$24^+ \rightarrow 23^+$	10.0(1)	0.84(10)	−0.15(7)	$M1+E2$
510.8(2)	3594.3	$23^+ \rightarrow 21^+$	16.8(3)	1.17(16)	0.06(1)	$E2$
510.8(4)	3672.8	$24^- \rightarrow 22^-$	12.5(2)	1.02(4)	0.05(2)	$E2$
513.3(18)	4911.3	$27^- \rightarrow 26^-$	3.0(2)	0.82(9)		$M1+E2$
538.6(2)	5449.9	$(28^-) \rightarrow 27^-$	3.1(1)	1.08(31)	−0.10(32)	$(M1+E2)$
546.9(1)	3594.3	$23^+ \rightarrow 22^+$	27.7(2)	0.82(4)	−0.11(2)	$M1+E2$
547.3(1)	2864.9	$19^- \rightarrow 17^-$	10.4(1)	1.08(7)	0.02(3)	$E2$
577.0(7)	6227.6	$32^+ \rightarrow 30^+$	2.0(1)	1.18(20)	0.33(10)	$E2$
585.4(2)	3228.8	$21^+ \rightarrow 19^+$	9.2(2)	1.22(26)	0.24(12)	$E2$
630.7(1)	5708.2	$29^- \rightarrow 28^-$	1.5(1)	0.94(18)		$M1+E2$
639.6(1)	3538.4	$22^+ \rightarrow 20^+$	11.6(2)	1.23(31)	0.12(10)	$E2$
648.8(5)	4436.3	$25^+ \rightarrow 24^+$	3.5(1)	1.58(53)	−0.23(21)	$M1+E2$
677.9(1)	5650.6	$30^+ \rightarrow 28^+$	3.3(1)	1.05(16)	0.23(7)	$E2$
679.5(5)	5077.5	$28^- \rightarrow 26^-$	2.2(1)	0.90(13)	0.08(6)	$E2$
689.2(9)	4476.7	$25^+ \rightarrow 24^+$	5.7(1)	1.07(16)	−0.12(10)	$M1+E2$

TABLE I. (*Continued.*)

E_γ (keV)	E_i (keV)	$I_i^\pi \rightarrow I_f^\pi$	I (ΔI)	R_{DCO} (ΔR_{DCO})	A_{pol} (ΔA_{pol})	Multipolarity
708.1(1)	1547.7	$15^- \rightarrow 13^-$	31.9(4)	1.09(4)	0.08(2)	$E2$
720.7(1)	1820.1	$16^- \rightarrow 14^-$	37.5(3)	0.95(5)	0.11(2)	$E2$
733.0(5)	4271.4	$24^+ \rightarrow 22^+$	7.2(2)	1.25(42)	0.48(13)	$E2$
740.1(1)	3787.5	$24^+ \rightarrow 22^+$	18.9(2)	1.30(11)	0.26(5)	$E2$
754.4(6)	3983.2	$23^+ \rightarrow 21^+$	3.2(1)	1.34(31)	0.26(21)	$E2$
769.9(3)	2317.6	$17^- \rightarrow 15^-$	17.5(2)	1.12(10)	0.07(4)	$E2$
788.7(1)	2608.8	$18^- \rightarrow 16^-$	25.9(2)	1.17(8)	0.15(3)	$E2$
795.1(3)	4467.9	$26^- \rightarrow 24^-$	8.5(2)	1.24(23)	0.05(4)	$E2$
796.9(4)	5708.2	$29^- \rightarrow 27^-$	6.5(1)	1.08(14)	0.13(7)	$E2$
842.0(13)	4436.3	$25^+ \rightarrow 23^+$	7.5(1)	1.17(8)	0.15(3)	$E2$
852.2(3)	4639.7	$26^+ \rightarrow 24^+$	12.8(1)	1.15(23)	0.06(3)	$E2$
864.1(1)	1963.5	$15^+ \rightarrow 14^-$	122.0(7)	0.76(3)	0.03(1)	$E1$
871.2(6)	5339.1	$28^- \rightarrow 26^-$	7.3(1)	1.31(24)	0.22(13)	$E2$
882.4(12)	4476.7	$25^+ \rightarrow 23^+$	4.1(1)	1.21(22)	0.44(16)	$E2$
925.9(1)	4911.3	$27^- \rightarrow 25^-$	9.9(1)	1.12(12)	0.12(6)	$E2$
928.7(3)	3976.1	$24^+ \rightarrow 22^+$	7.8(1)	1.12(12)	0.06(5)	$E2$
959.0(1)	4746.5	$26^+ \rightarrow 24^+$	3.5(1)	1.32(33)	0.18(10)	$E2$

[a]This transition was confirmed in the electron spectrum of the previous work [21].
[b]Multipolarities are taken from Ref. [21].

and the DCO analysis allows the deduction of the reduced transition probabilities $B(M1)/B(E2)$ in the $\pi h_{11/2} \otimes \nu i_{13/2}$ rotational band, using the approach of Ref. [1]:

$$\frac{B(M1)}{B(E2)} = 0.0693 \frac{16\pi}{5} \frac{E_\gamma^5(I \rightarrow I-2)}{E_\gamma^3(I \rightarrow I-1)\lambda(1+\delta^2)} \frac{(e\hbar/2Mc)^2}{e^2b^2} \quad (3)$$

where the energies of the γ-ray transitions are given in MeV. In most of the cases, the experimental DCO ratios of the mixed $M1/E2$ transitions take valuesthat are close to the limit for a stretched transition, with the exception of the 146.2- and 497.5-keV transitions. Therefore, $\delta = 0$ was set in the calculation. For the 146.2- and 497.5-keV transitions, the $B(M1)/B(E2)$ ratios take values of 1.24(1) and 1.12(1). If

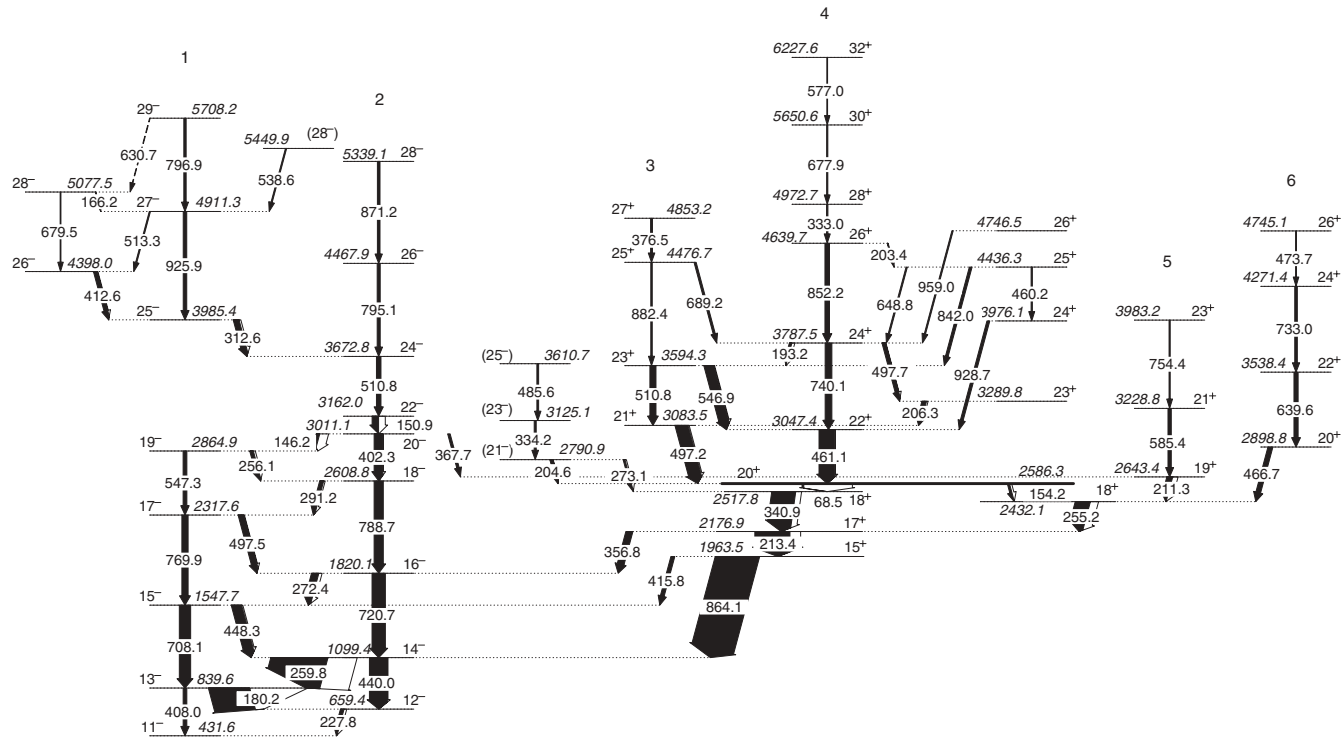

FIG. 1. Level scheme of ^{192}Au as obtained from the present work. The energies are in keV. The thicknesses of the arrows corresponds to the γ-ray intensities.

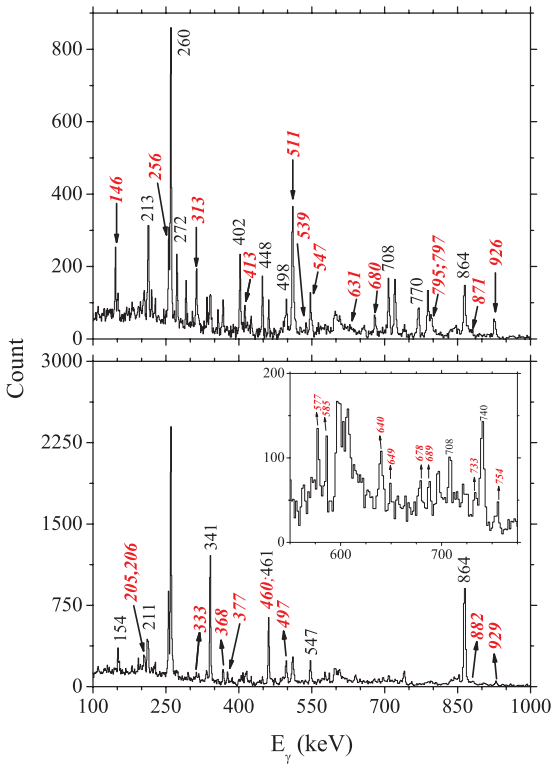

FIG. 2. (Color online) Top: Spectrum revealing the γ-ray transitions in negative parity states double gated on the 408.0 and 150.9 keV γ rays. Bottom: Spectrum revealing the γ-ray transitions in positive parity states double gated on the 213.4 and 408.0 keV γ rays. The expanded spectrum between 500 and 800 keV is shown on the right at the top of the figure. Newly observed transitions are indicated with arrows.

we accept $\delta \neq 0$, this will push these values down and will not change the trend and the conclusions.

The deduced $B(M1)/B(E2)$ ratios of reduced transition probabilities are given in Table II. In Fig. 3 the $B(M1)/B(E2)$ ratios for the 11^- bands in ^{190,192}Au are displayed. The

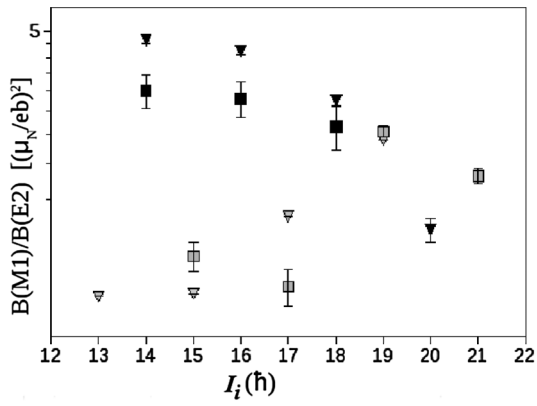

FIG. 3. The $B(M1)/B(E2)$ ratios of reduced transition probabilities for the $\pi h_{11/2}^{-1} \otimes \nu i_{13/2}^{-1}$ bands in ^{190,192}Au. The values for ^{190,192}Au are denoted by squares and triangles, respectively. The values for favored and unfavoed sequences are shown with empty and filled symbols, respectively.

TABLE II. Intensity branching ratios λ and ratios of reduced transition probabilities, $B(M1)/B(E2)$, for the 11^-, $\pi h_{11/2}^{-1} \otimes \nu i_{13/2}^{-1}$ band in ^{192}Au.

$I_i^\pi \rightarrow I_f^\pi$	E_γ (keV)	λ	$B(M1)/B(E2)$
$13^- \rightarrow 11^-$	408.0(1)	1.99(1)	0.68(1)
$13^- \rightarrow 12^-$	180.2(1)		
$14^- \rightarrow 12^-$	440.0(1)	0.14(1)	4.68(2)
$14^- \rightarrow 13^-$	259.8(1)		
$15^- \rightarrow 13^-$	708.1(1)	1.99(1)	0.69(1)
$15^- \rightarrow 14^-$	448.3(1)		
$16^- \rightarrow 14^-$	720.7(1)	1.56(1)	4.30(2)
$16^- \rightarrow 15^-$	272.4(1)		
$17^- \rightarrow 15^-$	769.9(1)	1.24(1)	1.24(1)
$17^- \rightarrow 16^-$	497.5(1)		
$18^- \rightarrow 16^-$	788.7(2)	2.90(2)	2.96(2)
$18^- \rightarrow 17^-$	291.2(1)		
$19^- \rightarrow 17^-$	547.3(1)	0.93(1)	2.20(2)
$19^- \rightarrow 18^-$	256.1(1)		
$20^- \rightarrow 18^-$	402.3(1)	2.10(1)	1.12(1)
$20^- \rightarrow 19^-$	146.2(1)		

$B(M1)/B(E2)$ ratios for ^{190}Au are deduced from the γ-ray intensities from Ref [17]. The favored and unfavored sequences are shown with empty and filled symbols respectively.

The results for both bands are very similar and display a well pronounced odd-even staggering, which vanishes in the backbending region.

Recently, the effect of odd-even staggering of the $B(M1)/B(E2)$ ratios in rotational bands in doubly-odd nuclei was discussed in relation to chiral rotation [25]. Chiral bands were suggested to appear in atomic nuclei with triaxial shapes [26]. Examples for such bands were suggested in the mass $A \approx 130$ [27] and $A \approx 100$ [28] regions. The staggering of the $B(M1)/B(E2)$ ratios was described in the framework of several models [29–31] and all of them consider large values of the deformation parameter γ. Similarly, for the mass $A \approx 190$ nuclei ^{190,192}Au, large values of the deformation parameter γ are expected, based on the observed staggering of the in-band $B(M1)/B(E2)$ ratios.

IV. DISCUSSION

A. Negative parity states

In order to study the evolution of nuclear shapes in ^{192}Au we employed total Routhian surface (TRS) and cranked shell model (CSM) calculations [19] (see Table III for the labeling convention information for the Routhians used in the calculations). At low angular momenta in the $\pi h_{11/2}^{-1} \otimes \nu i_{13/2}^{-1}$ configuration ^{192}Au is expected to take triaxial shapes with deformations $\beta_2 = 0.14$, $\beta_4 = -0.04$ and $\gamma = -80°$, according to the TRS calculations which are shown in Fig. 4. In the top panel of Fig. 4, potential energy surfaces for the eA sequence are shown for different frequencies. A potential minimum is displayed in (a) at $\gamma = -73.5°$ ($I = 17.8$) below the band crossing and in (b) at $\gamma = -68°$ ($I = 25.7$) above the band crossing. In the bottom panel of Fig. 4, the potential

TABLE III. Notations for the Routhians that are used in the text. Single-particle labels are at $\hbar\omega = 0$.

Notation	Signature label	Single-particle label
A	$(+,+1/2)$	$\nu i_{13/2}$
B	$(+,-1/2)$	$\nu i_{13/2}$
C	$(+,+1/2)$	$\nu i_{13/2}$
D	$(+,-1/2)$	$\nu i_{13/2}$
E	$(-,-1/2)$	$\nu h_{9/2}$
F	$(-,-1/2)$	$\nu h_{9/2}$
e	$(-,-1/2)$	$\pi h_{11/2}$
f	$(-,+1/2)$	$\pi h_{11/2}$

energy surfaces for the eB sequence are shown for different frequencies. A potential minimum is displayed in (c) at $\gamma = -82.3^\circ$ ($I = 11.8$) and in (d) at $\gamma = -69^\circ$ ($I = 23.4$) above the band crossing.

The calculations reproduce very well the observed band crossing for these sequences, which are displayed in Fig. 5. Alignment plots and experimental Routhians for eA and eB sequences in ^{192}Au are shown in the top and the bottom panels of Fig. 5. Harris parameters of $J_0 = 6\hbar^2$ MeV^{-1} and $J_1 = 30\hbar^4$ MeV^{-3} for ^{192}Au are used. Such a set of Harris parameters was used also for ^{193}Au [32]. A backbending with an alignment gain of $\Delta i \approx 11\hbar$ occurs in the negative parity band in ^{192}Au at rotational frequency $\hbar\omega_c \approx 0.26$ MeV, in good agreement with the TRS calculations, where an alignment gain of $12\hbar$ is obtained at a rotational frequency $\hbar\omega_c \approx 0.2$ MeV. A backbending at similar frequencies and with similar alignment gain is observed throughout this region, e.g., for the neighboring doubly-odd $^{190-194}$Hg [33] and $^{186-190}$Au [17,34] and even-even ^{190,192}Pt [32,35,36]. In

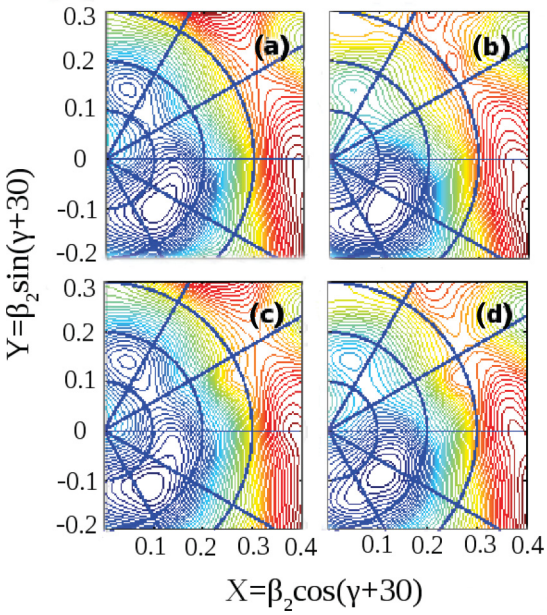

FIG. 4. (Color online) TRS plots for ^{192}Au calculated below and above the band crossing for sequence 1 at $\hbar\omega = 0.2$ MeV (a) and $\hbar\omega = 0.32$ MeV (b), and for sequence 2 at $\hbar\omega = 0.16$ MeV (c) and $\hbar\omega = 0.28$ MeV (d).

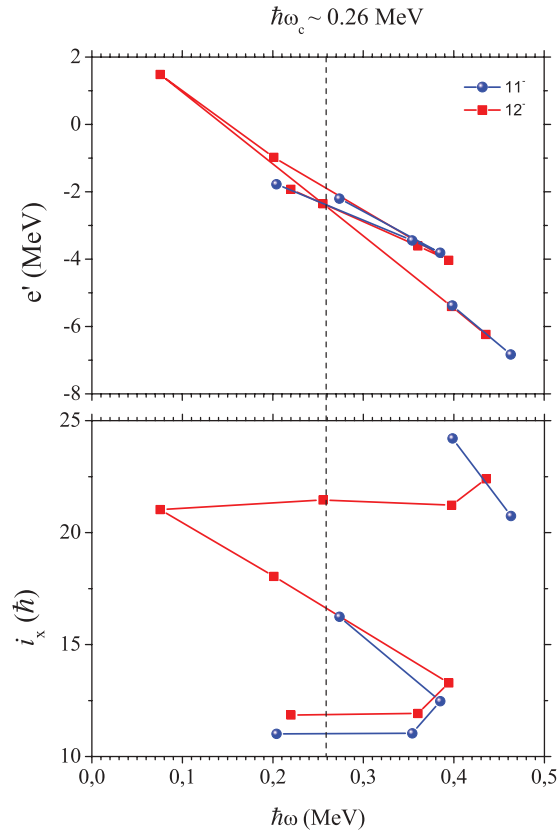

FIG. 5. (Color online) The experimental alignments (top) and the Routhians (bottom) vs rotational frequency for the 11^- and 12^- bands in ^{192}Au, calculated with $K = 0$ and Harris parameters of $J_0 = 6\hbar^2$ MeV^{-1} and $J_1 = 30\hbar^4$ MeV^{-3}. The vertical line indicates the position of the band crossing.

Fig. 5 the 925.9-keV transition ($I_i^\pi = 27^-$) is consistent with the trend in the favored sequence. Note, however, that two transitions in the unfavored sequence between $I^\pi = 19^-$ and $I^\pi = 25^-$ were not observed.

CSM calculations were performed for ^{192}Au using deformations, obtained by averaging the values for the TRS minima, e.g., $\beta_2 = 0.14$, $\beta_4 = -0.04$, and $\gamma = -80^\circ$. In Fig. 6, the neutron quasiparticle Routhians are plotted. A Woods-Saxon potential with universal parameters is used. The first AB crossing (at $\hbar\omega_c \approx 0.2$ MeV, indicated by arrow in the figure) is blocked in the $\pi h_{11/2}^{-1} \otimes \nu i_{13/2}^{-1}$ configuration and the second BC crossing is predicted to occur a little higher in frequency, $\hbar\omega_c \approx 0.27$ MeV, in perfect agreement with the experiment.

Sequences 1 and 2 in Fig. 1 are assigned to the rotational aligned $\pi h_{11/2}^{-1} \otimes \nu i_{13/2}^{-1}$ configuration [16]. The experimental results show good agreement with the set of eA and eB rotation-aligned bands in theoretical calculations.

The TRS calculations indicate that the $\pi h_{11/2} \otimes \nu i_{13/2}$ sequence is built on triaxial shape ($\gamma \approx -80^\circ$). The alignment of a pair of quasineutrons drives the shape to oblate ($\gamma \approx -68^\circ$). This is in agreement with the observed large scattering of the $B(M1)/B(E2)$ ratios below the band crossing, which diminishes in the crossing region.

The $\pi h_{11/2}^{-1} \otimes \nu i_{13/2}^{-1}$ bands show signature inversion in the $N = 107$–113 Au isotopes [34]. With the increase of

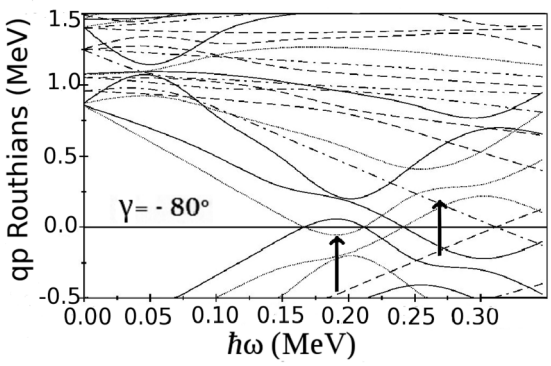

FIG. 6. Cranked shell model calculations for ^{192}Au for neutrons with deformations of $\beta_2 = 0.14$, $\beta_4 = -0.04$, and $\gamma = -80^\circ$. The Routhians with $(\pi, \alpha) = (+, +1/2)$ are represented with a solid line, $(+, -1/2)$ with a dotted line, $(-, +1/2)$ with a dash-dotted line, and $(-, -1/2)$ with a dashed line.

the neutron number triaxial deformations become more pronounced. γ softness and triaxiality have been discussed for the low-lying states of the heavier Au isotopes [17,32,34,37,38]. The observed signature inversions in the $\pi h_{11/2} \otimes \nu i_{13/2}$ bands of ^{188,190}Au were reproduced by CSM calculations taking into account the nonaxial shape with $\gamma \leqslant -70^\circ$ [17,37,38]. In ^{192}Au CSM calculations for $\gamma = -80^\circ$ reproduced the observed signature inversion too (see Fig. 6).

B. Positive parity states

The 15^+ states in the doubly-odd ^{190,192,194}Au nuclei are assigned to the $\pi h_{11/2}^{-1} \otimes \nu i_{13/2}^{-2} j$, $j = (p_{3/2}, f_{5/2})$ configuration [16]. The 20^+ isomers in ^{190,192}Au [21] decay to these states.

Two positive-parity sequences (denoted as 3 and 4 in Fig. 1) were observed on top of the 20^+ isomer, which is assigned to the $\pi h_{11/2}^{-1} \otimes \nu i_{13/2}^{-2} h_{9/2}^{-1}$ configuration [21]. Similar sequences have been observed in the neighboring ^{190}Au [17]. Based on TRS calculations these bands were assigned to the eFAB, eFAC, and eFBC configurations. In the case of ^{192}Au, in most of the sequences only two or three transitions were observed. More transitions were observed in sequence 4. Based on the similarities of the excitation energies of the levels in this sequence to these in sequence (d) in ^{190}Au [17], we suggest that it has the eFBC configuration. Similarly, based on the decay pattern, sequence 3 can be associated with the eFAC configuration.

Parallel to these, two more sequences with positive parity were observed, denoted 5 and 6 in Fig. 1. Similar semidecoupled structures were observed in ^{190}Au as well. They are understood to take the $\pi h_{11/2}^{-1} \otimes \nu i_{13/2}^{-2} j$, $j = (p_{3/2}, f_{5/2})$ configuration [17]. In ^{192}Au we suggest that sequences 5 and 6 have the same structure.

V. CONCLUSIONS

In summary, the level scheme of ^{192}Au was extended up to $I^\pi = 32^+$ and an excitation energy of $\sim$6 MeV. Rotational sequences, which are built on triaxial shapes ($\gamma \approx -80^\circ$), were established. The negative parity rotation-aligned $\pi h_{11/2}^{-1} \otimes \nu i_{13/2}^{-1}$ band was extended beyond the band crossing region. TRS calculations and experimental $B(M1)/B(E2)$ ratios indicate that the alignment of a pair of $\nu i_{13/2}$ quasineutrons drives the shape towards oblate (from $\gamma \approx -80^\circ$ to $\gamma \approx -70^\circ$). Several sequences with positive parity were observed, which are associated with four-quasiparticle excitations. TRS and CSM calculations were performed to study the presence of nonaxiality of ^{192}Au. The agreement between experiment and calculations indicated that ^{192}Au nucleus shows nonaxial deformations with $-68^\circ \leqslant \gamma \leqslant -82^\circ$ similar to the other Au nuclei in $A \approx 190$ region.

ACKNOWLEDGMENTS

The Sofia and Istanbul groups thank WNSL for the excellent working conditions. This work is supported by the US DOE under Grants No. DE-FG02-91ER-40609 and No. DE-FG05-96ER40983, by the Scientific Research Projects Coordination Unit of Istanbul University under Project No. 5808, by the Turkish Atomic Energy Authority under Projects No. DPT-04K120100-4 and No. CERN-A5.H2.P1.01-4, and by the the Bulgarian Science Fund, Project No. DID-02/16. R.B.C. thanks the Humboldt Foundation for support.

[1] A. Bohr and B. R. Mottelson, *Nuclear Structure*, Vol. 2 (Benjamin, Reading, 1975).
[2] C. Bourgeois, M. G. Porquet, N. Perrin, H. Sergolle, F. Hannachi, G. Bastin, and F. Beck, Z. Phys. A **333**, 5 (1989).
[3] J. K. Johansson, D. G. Popescu, D. D. Rajnauth, J. C. Waddington, M. P. Carpenter, L. H. Courtney, V. P. Janzen, A. J. Larabee, Z. M. Liu, and L. L. Riedinger, Phys. Rev. C **40**, 132 (1989).
[4] N. Perrin, A. Korichi, C. Bourgeois, F. Azaiez, J. Duprat, F. Ibrahim, D. Hojman, F. Le Blanc, D. G. Popescu, and H. Sergolle, Z. Phys. A **347**, 81 (1993).
[5] T. Bengtsson and I. Ragnarsson, Nucl. Phys. A **436**, 14 (1985).
[6] G. Hebbinghaus, W. Gast, A. Kramer-Flecken, R. M. Lieder, J. Skalski, and W. Urban, Z. Phys. A **328**, 387 (1987); G. Hebbinghaus, T. Kutsarova, W. Gast, A. Kramer-Flecken, R. M. Lieder, and W. Urban, Nucl. Phys. A **514**, 225 (1990).
[7] F. Hannachi *et al.*, Nucl. Phys. A **481**, 135 (1988).
[8] R. Bengtsson, T. Bengtsson, J. Dudek, G. Leander, W. Nazarewicz, and J.-y. Zhang, Phys. Lett. B **183**, 1 (1987).
[9] W. Nazarewicz, M. A. Riley, and J. D. Garrett, Nucl. Phys. A **512**, 61 (1990).
[10] Th. Hilberath, St. Becker, G. Bollen, H.-J. Kluge, U. Kronert, G. Passler, J. Rikovska, and R. Wyss (ISOLDE Collaboration), Z. Phys. A **342**, 1 (1992).
[11] J. Rikovska, R. Wyss, and P. B. Semmes, Hyperfine Interact. **75**, 59 (1992).
[12] P. Sarriguren, R. Rodriguez-Guzman, and L. M. Robledo, Phys. Rev. C **77**, 064322 (2008).
[13] P. D. Stevenson, M. P. Brine, Zs. Podolyak, P. H. Regan, P. M. Walker and J. R. Stone, Phys. Rev. C **72**, 047303 (2005).

[14] P. D. Bond, R. F. Casten, D. D. Warner, and D. Horn, Phys. Lett. B **130**, 167 (1983).
[15] J. A. Cizewski, R. F. Casten, G. J. Smith, M. L. Stelts, W. R. Kane, H. G. Börner, and W. F. Davidson, Phys. Rev. Lett. **40**, 167 (1978); R. F. Casten and J. A. Cizewski, Nucl. Phys. A **309**, 477 (1978).
[16] A. Neskakis, R. M. Lieder, H. Beuscher, Y. Gono, D. R. Haenni, and M. Müller-Veggian, Nucl. Phys. A **390**, 53 (1982).
[17] E. Gueorguieva, C. Schück, A. Minkova, Ch. Vieu, M. Kaci, F. Hannachi, R. Wyss, J. S. Dionisio, A. Korichi, and A. Lopez-Martens, Phys. Rev. C **69**, 044320 (2004).
[18] H. L. Yadav, H. Toki, and A. Faessler, Phys. Lett. B **81**, 119 (1979).
[19] R. Wyss, W. Satula, W. Nazarewicz, and A. Johnson, Nucl. Phys. A **511**, 324 (1990).
[20] W. Nazarewicz, G. A. Leander, and J. Dudek, Nucl. Phys. A **467**, 437 (1987).
[21] E. Gueorguieva *et al.*, Phys. Rev. C **64**, 064304 (2001).
[22] C. W. Beausang *et al.*, Nucl. Instrum. Methods A **452**, 431 (2000).
[23] D. C. Radford, Nucl. Instrum. Methods A **361**, 297 (1995); http://radware.phy.ornl.gov.
[24] G. Duchene, F. A. Beck, P. J. Twin, G. de France, D. Curien, L. Han, C. W. Beausang, M. A. Bentley, P. J. Nolan, and J. Simpson, Nucl. Instrum. Methods A **432**, 90 (1999).
[25] T. Koike, K. Starosta, C. J. Chiara, D. B. Fossan, and D. R. LaFosse, Phys. Rev. C **67**, 044319 (2003).
[26] S. Frauendorf and J. Meng, Nucl. Phys. A **617**, 131 (1997).
[27] K. Starosta *et al.*, Phys. Rev. Lett. **86**, 971 (2001).
[28] C. Vaman, D. B. Fossan, T. Koike, K. Starosta, I. Y. Lee, and A. O. Macchiavelli, Phys. Rev. Lett. **92**, 032501 (2004).
[29] B. Qi, S. Q. Zhang, S. Y. Wang, J. Meng, and T. Koike, Phys. Rev. C **83**, 034303 (2011); J. Peng, J. Meng, and S. Q. Zhang, *ibid.* **68**, 044324 (2003).
[30] T. Koike, K. Starosta, and I. Hamamoto, Phys. Rev. Lett. **93**, 172502 (2004).
[31] H. G. Ganev, A. I. Georgieva, S. Brant, and A. Ventura, Phys. Rev. C **79**, 044322 (2009); H. G. Ganev and S. Brant, *ibid.* **82**, 034328 (2010).
[32] Y. Oktem *et al.*, Phys. Rev. C **76**, 044315 (2007).
[33] H. Hübel, A. P. Byrne, S. Ogaza, A. E. Stuchbery, G. D. Dracoulis, and M. Guttormsen, Nucl. Phys. A **453**, 316 (1986).
[34] V. P. Janzen *et al.*, Phys. Rev. C **45**, 613 (1992).
[35] J. C. Cunnane, M. Piiparinen, P. J. Daly, C. L. Dors, T. L. Khoo, and F. M. Bernthal, Phys. Rev. C **13**, 2197 (1976).
[36] S. A. Hjorth, A. Johnson, Th. Lindblad, L. Funke, P. Kemnitz, and G. Winter, Nucl. Phys. A **262**, 328 (1976).
[37] E. Gueorguieva *et al.*, Phys. Rev. C **68**, 054308 (2003).
[38] Y. D. Fang *et al.*, Phys. Rev. C **82**, 064303 (2010).